Electronic Supplementary Information

Ternary-salt gel polymer electrolyte for anode-free lithium metal batteries with an untreated Cu substrate

Yu-Hsing Lin,[a] *Chun−Yan Shih,*[a] *Ramesh Subramani,*[a] *Yuh-Lang Lee,*[a,b] *Jeng-Shiung Jan,*[a,b] *Chi-Cheng Chiu,*[a,b] *and Hsisheng Teng*[a,b,c,*]

[a]Department of Chemical Engineering, National Cheng Kung University, Tainan 70101, Taiwan

[b]Hierarchical Green-Energy Materials (Hi-GEM) Research Center, National Cheng Kung University, Tainan 70101, Taiwan

[c]Center of Applied Nanomedicine, National Cheng Kung University, Tainan 70101, Taiwan

* Corresponding Author (E-mail: hteng@mail.ncku.edu.tw)

Supporting information for:

1. Interaction between DOL and anions

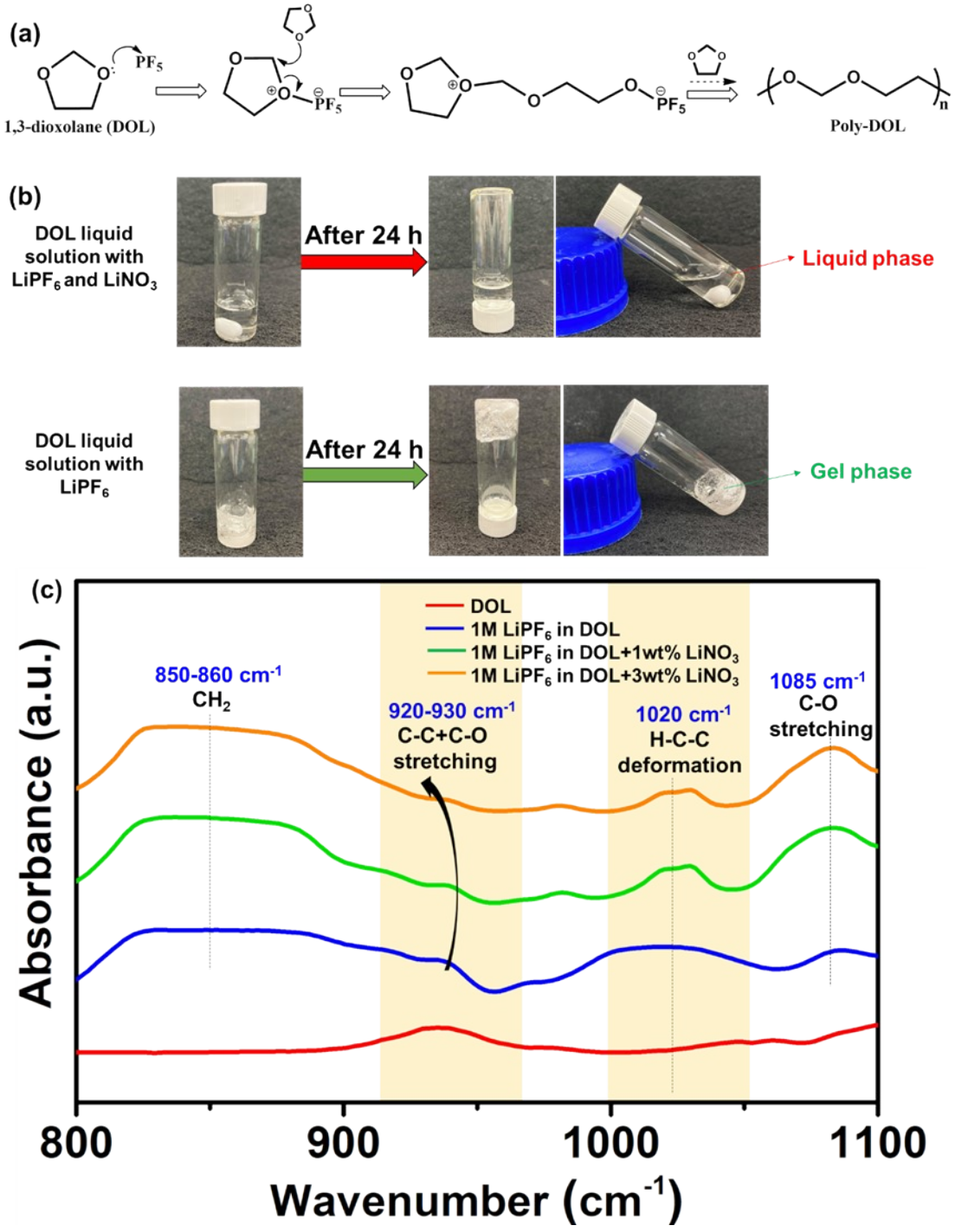

Fig. S1 (a) Schematic model of the mechanism of DOL polymerization induced by $LiPF_6$; (b) optical photographs of liquid solutions of $LiPF_6$ and DOL with and without $LiNO_3$; and (c) FTIR spectra of the produced electrolytes. The electrolytes were 1 M solution of $LiPF_6$ in the DOL solvent. We added different concentrations of $LiNO_3$ (1 and 3 wt%) to the produced electrolytes. FTIR measurements indicated that the addition of $LiPF_6$ and $LiNO_3$ to DOL

resulted in multiple changes (Fig. S1c). First, the peak corresponding to the vibration associated with H–C–C deformation (1020 cm^{-1}) split into two peaks, which indicated that cyclic DOL molecules were coordinated and underwent a shape change because of their interactions with $LiPF_6$ and $LiNO_3$. These interactions were stronger with the addition of $LiNO_3$. Second, the infrared peak located at approximately 920 cm^{-1}, which was assigned to C–C/C–O stretching on the ring, was observed in the presence of $LiPF_6$ but gradually disappeared and shifted to lower wavenumbers with an increase in the quantity of $LiNO_3$.

2. Nyquist impedance plots of the produced electrolytes

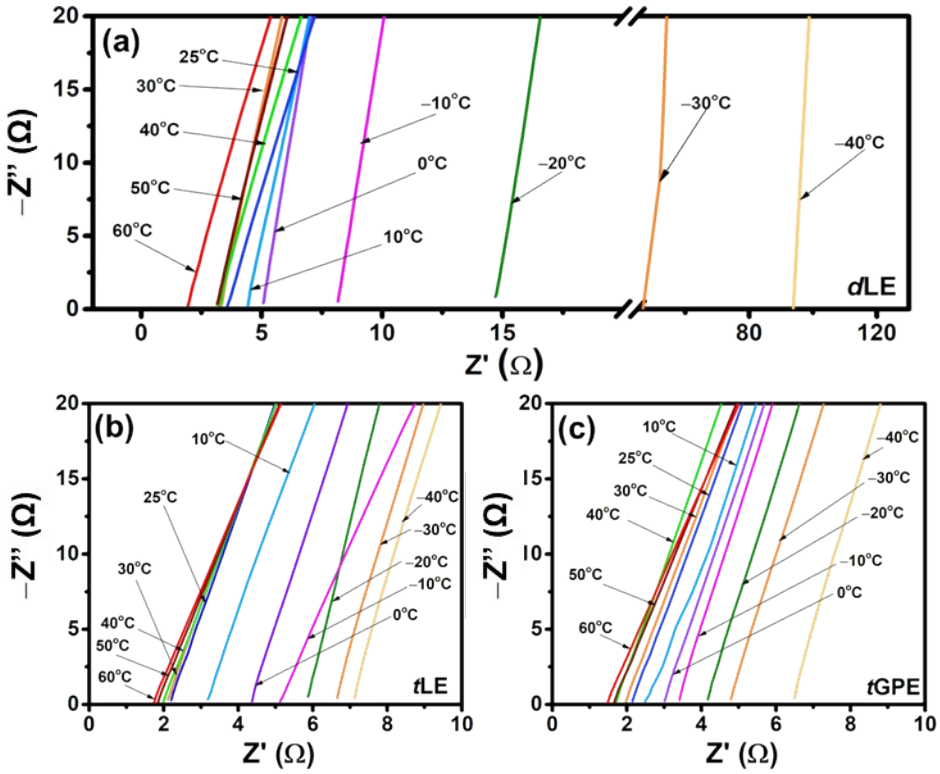

Fig. S2 Nyquist impedance plots of the separator-supported electrolytes sandwiched between two SS foils at various temperatures: (a) *d*LE, (b) *t*LE, and (c) *t*GPE. The analysis was conducted at 0 V with an AC potential amplitude of 10 mV over a frequency range of 100 mHz to 100 kHz. The ionic conductivity (σ) was calculated using the following equation: $\sigma = d/(R_I \times A)$, where d is the distance between the SS electrodes, R_I is the bulk resistance determined from the intercept on the real axis of the Nyquist plots, and A is the geometric area of the electrolyte–electrode interface.

3. Nucleation potential of Li in the *t*GPE, *t*LE, and *d*LE

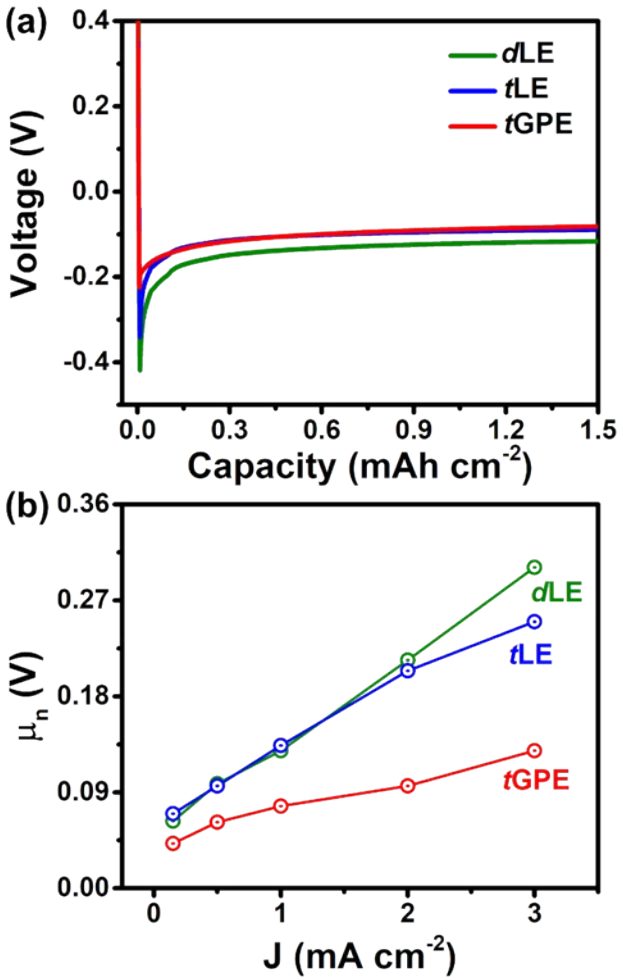

Fig. S3 Nucleation overpotentials measured using Li||Cu cells containing the *d*LE, *t*LE, and *t*GPE: (a) voltage–capacity curves during Li nucleation at a current density of 3 mA cm^{-2} and (b) Li nucleation overpotentials at different current densities (*J*).

4. SEM images of the Li plating–stripping progress in the *d*LE

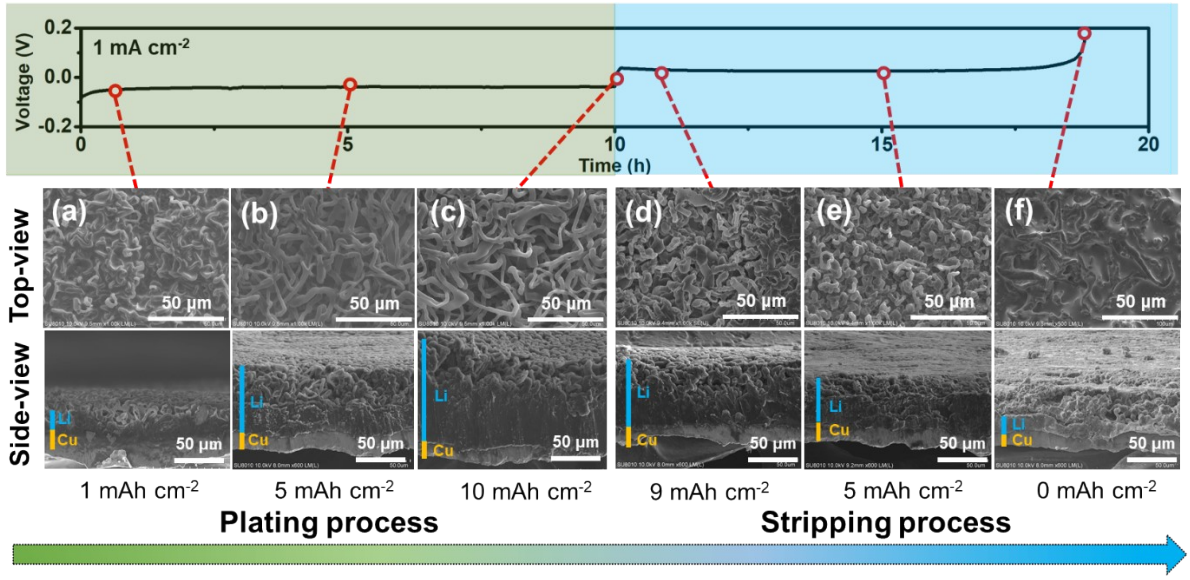

Fig. S4 Top- and side-view SEM images of Li deposits on the Cu substrate in the Li|*d*LE|Cu cell under plating–stripping at a current density of 1 mA cm^{-2}: Li plating under Li deposition capacities of (a) 1, (b) 5, and (c) 10 mAh cm^{-2} as well as Li stripping under Li deposition capacities of (d) 9, (e) 5, and (f) approximately 0 mAh cm^{-2}.

5. SEM images of the Li plating–stripping progress in the *t*LE

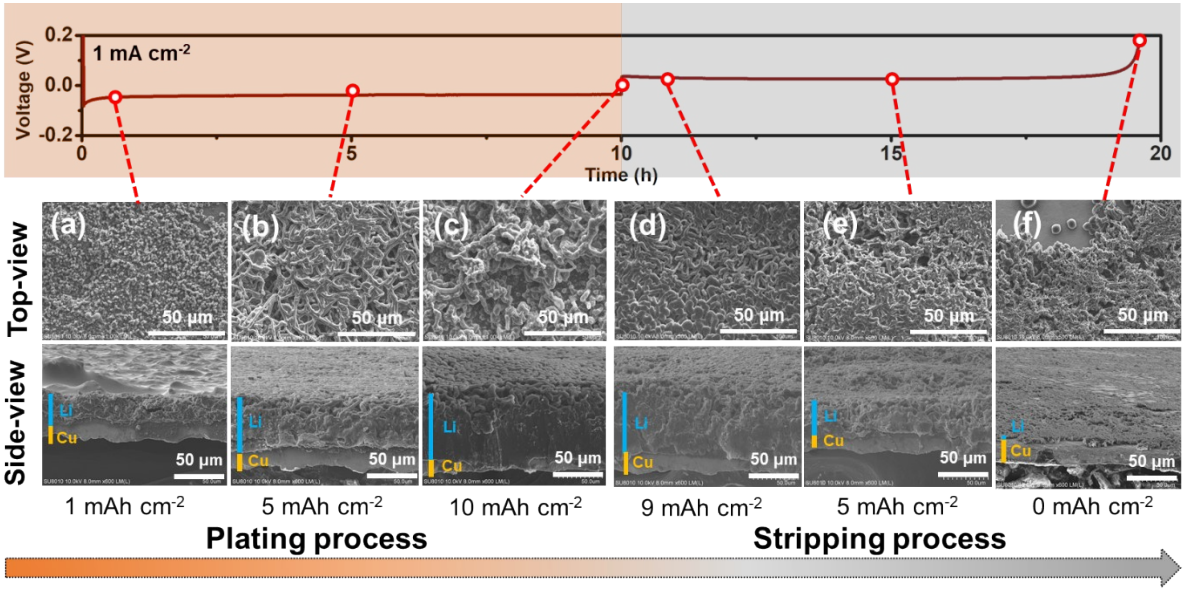

Fig. S5 Top- and side-view SEM images of Li deposits on the Cu substrate in the Li|*t*LE|Cu cell under plating–stripping at a current density of 1 mA cm^{-2}: Li plating under Li deposition capacities of (a) 1, (b) 5, and (c) 10 mAh cm^{-2} as well as Li stripping under Li deposition capacities of (d) 9, (e) 5, and (f) approximately 0 mAh cm^{-2}.

6. Cyclic voltammetry measurement for Li||Cu cells

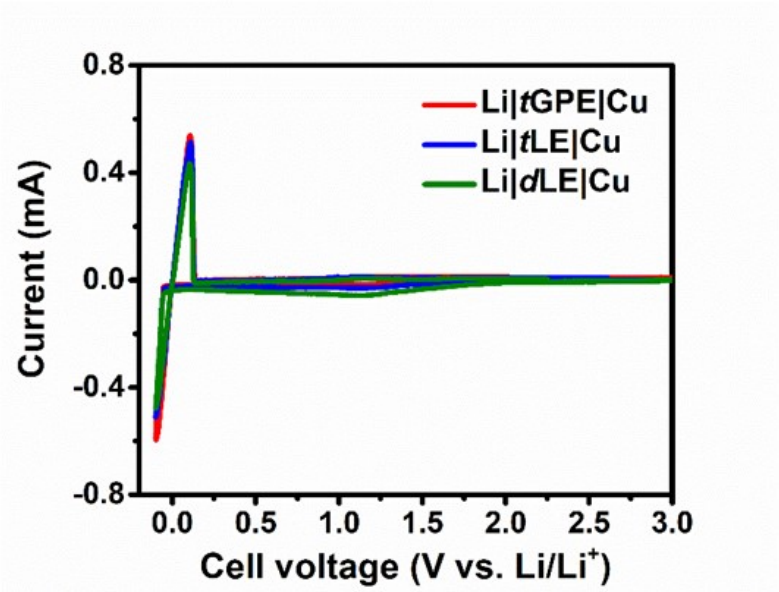

Fig. S6 Cyclic voltammetry (CV) of Li|*t*GPE|Cu, Li|*t*LE|Cu and Li|*d*LE|Cu in the voltage range of -0.1–3.0V. The corresponding comparison of redox peaks at the first cycle.

7. Cycling of Li||Cu cells under a current density of 0.5 mA cm^{-2}

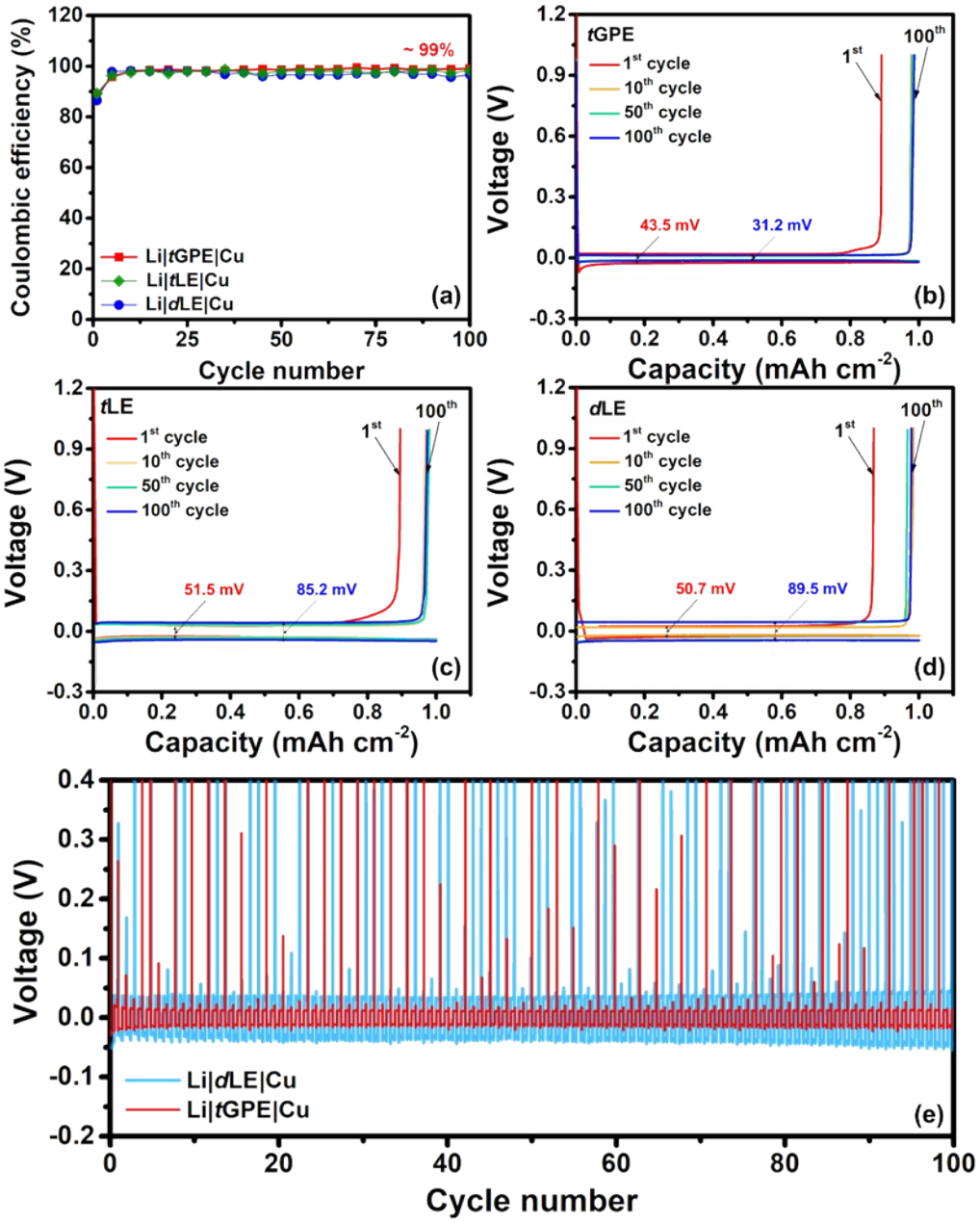

Fig. S7 Li plating–stripping cycling in Li||Cu cells under a current density of 0.5 mA cm^{-2} and a Li deposition capacity of 1 mAh cm^{-2}: (a) variation in the CEs of the cells assembled using the *t*GPE, *t*LE, and *d*LE during cycling; (b) voltage–capacity profiles of the Li|*t*GPE|Cu cell in different cycles; (c) voltage–capacity profiles of the Li|*t*LE|Cu cell in different cycles; (d) voltage–capacity profiles of the Li|*d*LE|Cu cell in different cycles; and (e) comparison of the voltage cycle profiles of the Li|*t*GPE|Cu and Li|*d*LE|Cu cells throughout the cycling.

8. Plating–stripping of Li||Li cells with the *d*LE and *t*GPE

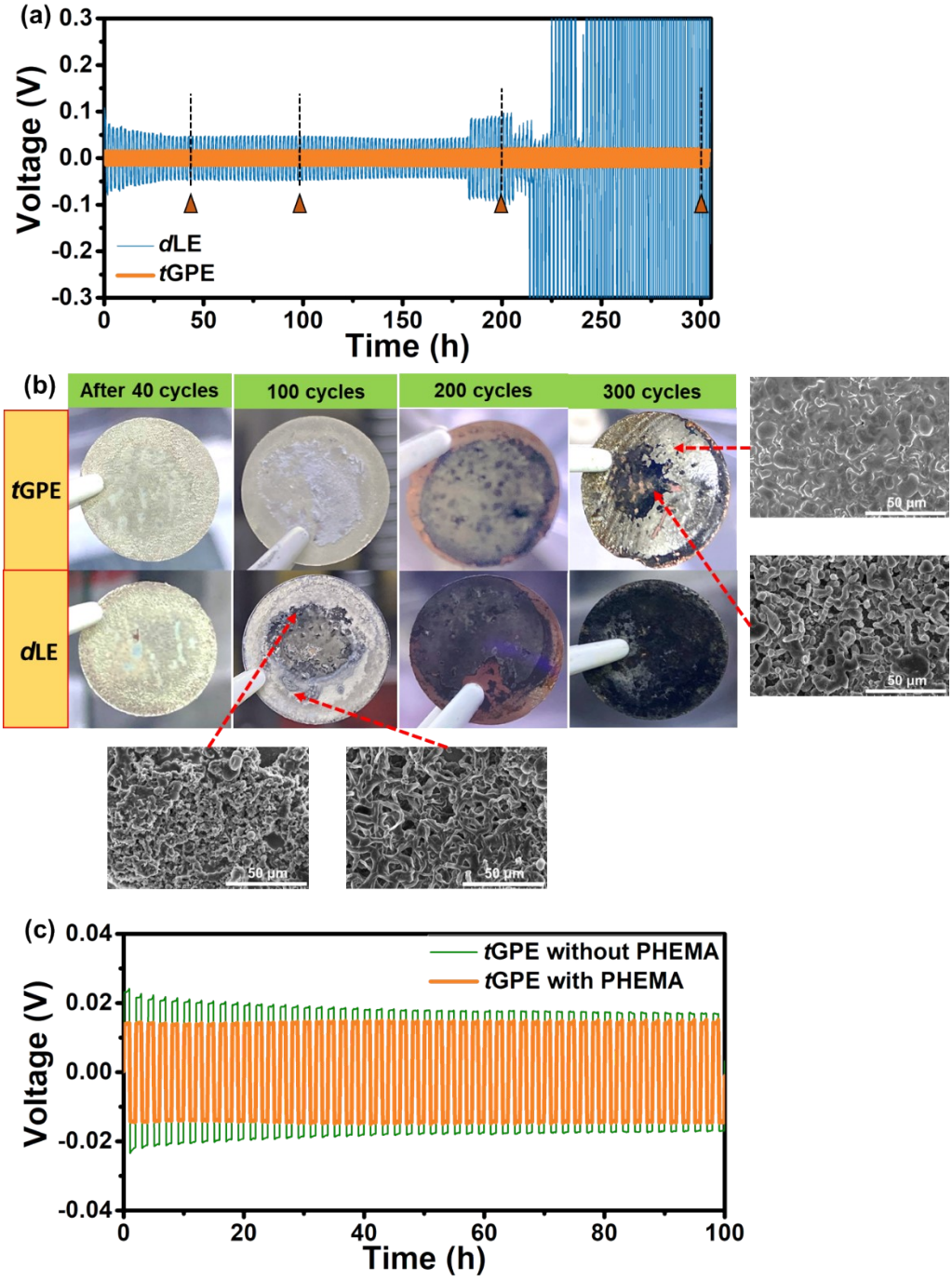

Fig. S8 Cyclic Li plating–stripping performance of Li||Li cells with Li@Cu electrodes having a capacity of 4 mAh cm^{-2}: (a) voltage profiles of the Li@Cu|*t*GPE|Li@Cu and Li@Cu|*d*LE|Li@Cu cells during Li plating–stripping at a current density of 1 mA cm^{-2} for 300 h and (b) optical images of Li@Cu electrodes after different cycles of plating–stripping

in the Li@Cu|*t*GPE|Li@Cu and Li@Cu|*d*LE|Li@Cu cells. (c) voltage profiles of the Li@Cu||Li@Cu cells, assembled using the *t*GPE and PHEMA-free *t*GPE, during Li plating–stripping at a current density of 1 mA cm^{-2} for 100 h. The SEM-image insets in panel (b) explains why the *t*GPE cell exhibited lower overpotential than did the *d*LE cell even though the Li@Cu electrode in the *t*GPE has dark areas at 300 h similar to Li@Cu electrode in the *d*LE at 100 h. For the electrode in the *t*GPE at 300 h, the shiny area exhibited dense and even Li deposition and the dark area contained some uneven Li deposits. By contrast, for the electrode in the *d*LE at 100 h, the shiny area contained dendritic Li deposits, which would have imposed high interfacial resistant for Li^+ transport. The dark area contained disarranged Li deposits covered with non-metallic species, likely produced from electrolyte decomposition.

9. Interaction between Naph and Li

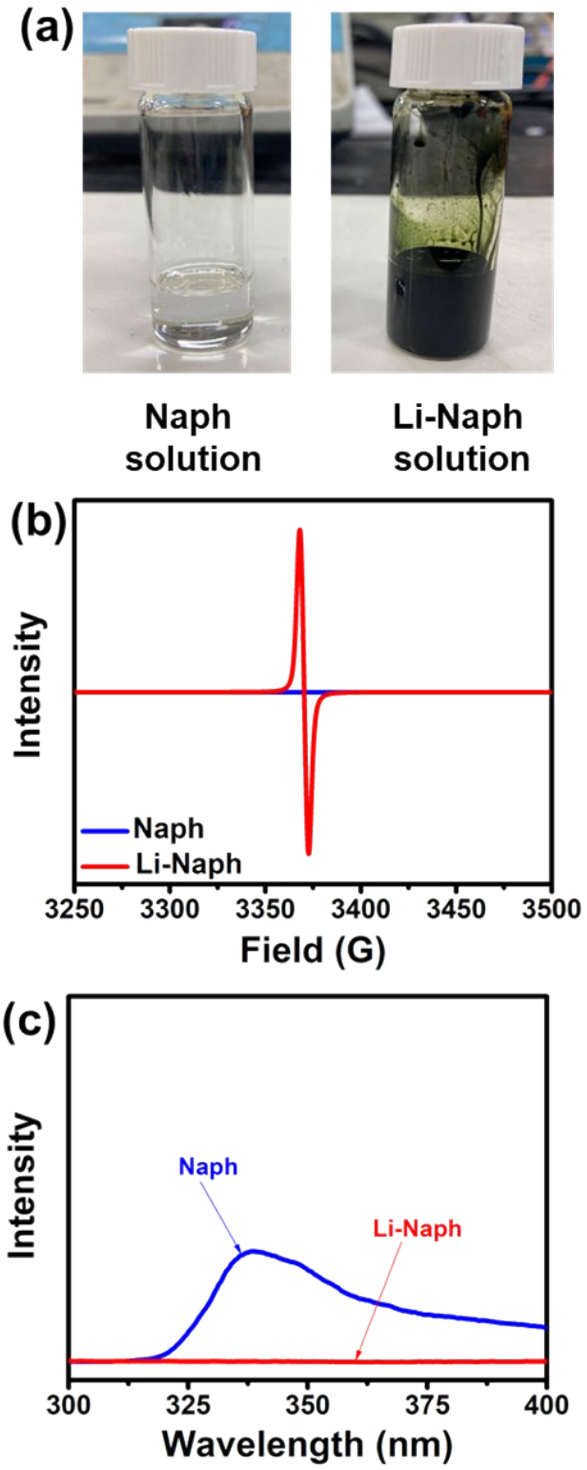

Fig. S9 (a) Optical graphs of 1 M Naph and 1 M Li-Naph solutions dissolved in DME; (b) EPR spectra of the Naph and Li-Naph solutions; and (c) emission spectra of 1 M Naph in DME before (blue) and after (red) Li treatment.

10. Active Li content of plated–stripped Li electrodes

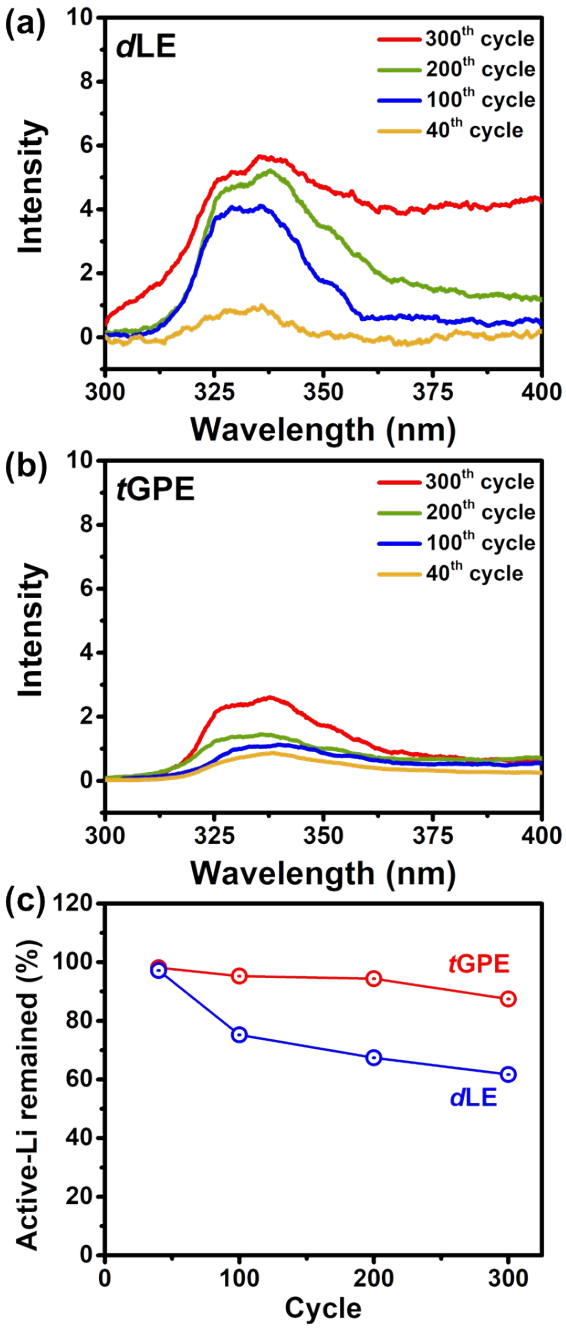

Fig. S10 Fluorescence intensity of the Naph solution dropped onto cycled electrodes that were disassembled after different numbers of plating-stripping cycles from the (a) Li@Cu|*d*LE|Li@Cu and (b) Li@Cu|*t*GPE|Li@Cu cells. (c) Variation in the proportion of active Li remained on the Li@Cu electrodes during cycling of the *d*LE and *t*GPE cells.

11. Quantitative analysis of active Li

According to the dependence of the fluorescence intensity on the Naph concentration (Fig. ESIa), a fluorescence–Naph concentration calibration curve was established. This curve is displayed in Fig. ESIb, with the fluorescence and Naph concentration having linear dependence. By fitting the data depicted in Fig. ESIb with Eq. (1), which represents the relationship between the fluorescence and Naph concentration, the values of the constants *a* and *b* were determined to be 13.5 M^{-1} and 0.834, respectively. On the basis of Eq. (1) and the fluorescence intensity results after 300 cycles (Fig. S8d), where the fluorescence intensity of the *d*LE and *t*GPE was 5.98 and 2.52, respectively, the remaining Naph concentration was determined to be 0.382 and 0.125 M for the *d*LE and *t*GPE, respectively.

$$\text{Fluorescence intensity} = b + a \times C_{\text{Naph}} \quad (1)$$

As presented in (R1), Li-Naph can be prepared by simply mixing stoichiometric quantities of Li and Naph in a molar ratio of 1:1 in DME solvent.

(R1)

We prepared a 1 M Naph solution, and 0.150 mL of this Naph solution was dropped onto the surface of the samples by using a micropipette. Fluorescence spectra were then recorded under excitation at 220 nm. By using Eq. (1), the consumed Naph concentration for the *d*LE and *t*GPE was calculated to be 0.619 and 0.875 M, respectively, which corresponded to the quantity of active Li consumed by Naph. Thus, the weight of active Li in the *d*LE and GPE after 300 cycles was determined as follows:

For the *d*LE: 0.619 M × 7.00 g mol^{-1} × 0.150 mL = 0.650 mg

For the *t*GPE: 0.875 M × 7.00 g mol^{-1} × 0.150 mL = 0.918 mg

To support the results obtained from the as-established Naph calibration curve and Eq. (1), we plotted the fluorescence of residual Naph ($FL_{\text{resid.}}$) against the quantity of Li on Cu (W_{Li}). We predeposited different quantities of Li on Cu and dropped 0.150 mL of Naph solution onto the surface of the samples. We then recorded fluorescence spectra under excitation at 220 nm. The parameters $FL_{\text{resid.}}$ and W_{Li} had linear dependence (Fig. ESIc), and the obtained data were fitted using Eq. (2). The values of the constants *c* and *d* were determined to be 12.6 and −10.2 mg^{-1}, respectively.

$$FL_{\text{resid.}} = c + d \times W_{\text{Li}} \quad (2)$$

The fluorescence intensity of the *d*LE and *t*GPE after 300 cycles was 5.98 and 2.52, respectively (Fig. S9a,b). Moreover, by using Eq. (2), the active Li content on Cu was

determined to be 0.649 and 0.988 mg for the *d*LE and *t*GPE, respectively. This result was consistent with that calculated from the fluorescence–Naph concentration plot, which indicates that the estimated values of residual active Li after 300 cycles were reliable.

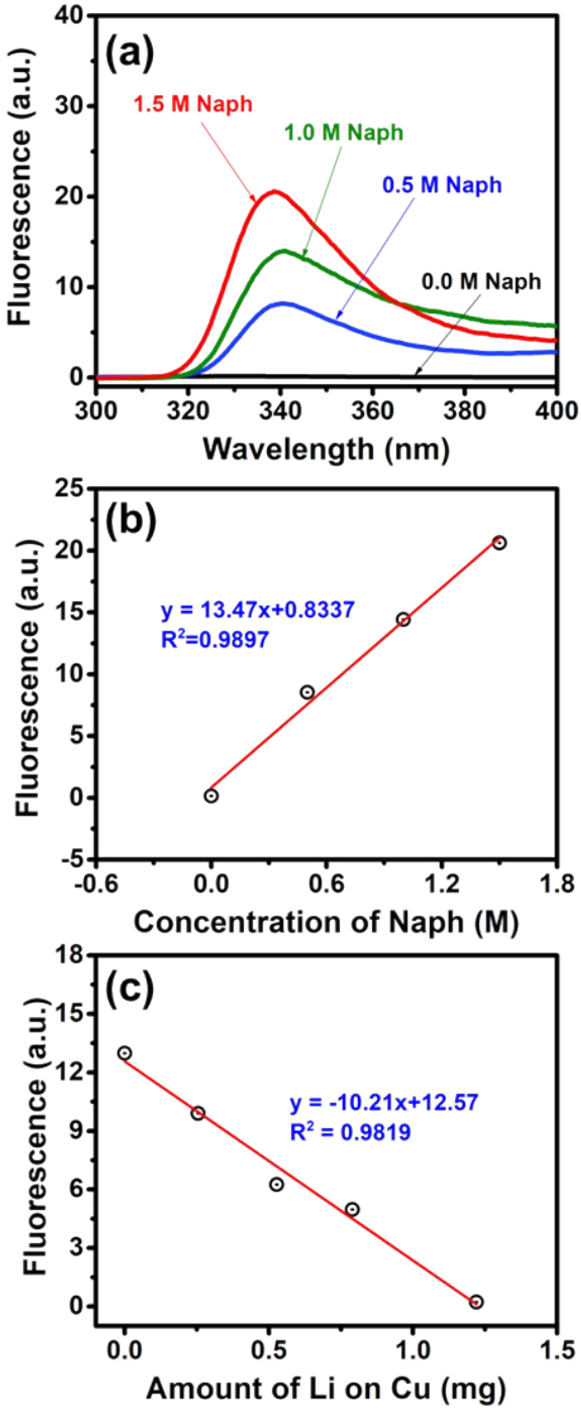

Fig. ESI (a) PL emission spectra of Naph solutions with different concentrations under 220-nm excitation; (b) linear fit of the PL emission intensity against the Naph concentration; and (c) linear fit of the PL emission intensity against the quantity of Li on Cu.

12. The interface resistances of the electrolytes measured by EIS test during the cycling

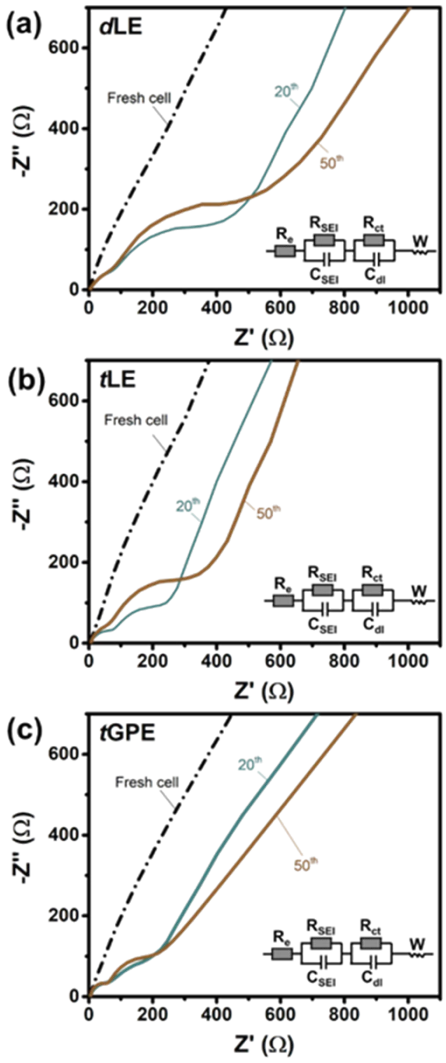

	Fresh	20th	50th
R_e	3.96 Ω	6.15 Ω	7.32 Ω
R_{SEI}	~0	46.2 Ω	58.3 Ω
R_{ct}	~0	200 Ω	250 Ω

	Fresh	20th	50th
R_e	4.01 Ω	4.15 Ω	4.89 Ω
R_{SEI}	~0	44.3 Ω	47.7 Ω
R_{ct}	~0	120 Ω	190 Ω

	Fresh	20th	50th
R_e	3.66 Ω	3.59 Ω	3.90 Ω
R_{SEI}	~0	40.3 Ω	42.6 Ω
R_{ct}	~0	95.2 Ω	110 Ω

Fig. S11 AC impedance complex-plane spectra of the anode-free cells before and after cycling for 20 and 50 cycles. (a) Cu|*d*LE|$LiFePO_4$, (b) Cu|*t*LE|$LiFePO_4$ and (c) Cu|*t*GPE|$LiFePO_4$.

13. Cycling performance of the Cu|*t*GPE|NMC_{532} AFLMB

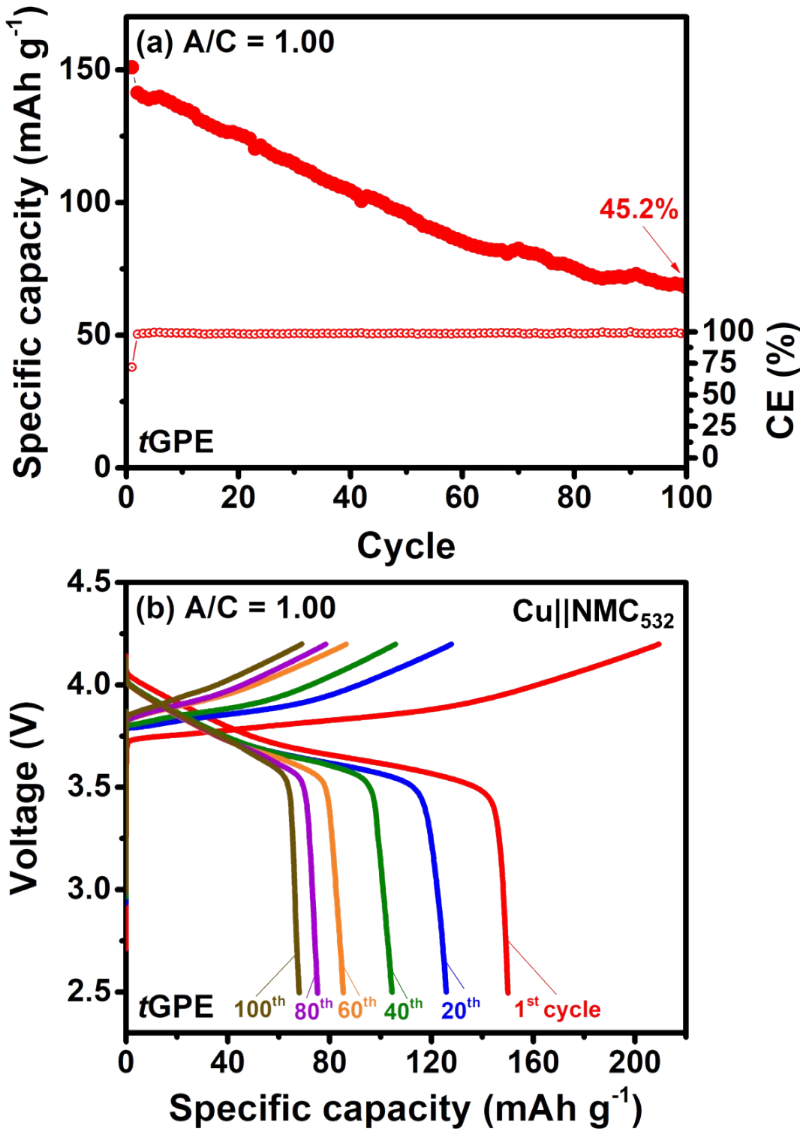

Fig. S12 Cycling performance of a Cu||NMC_{532} anode-free battery assembled using the *t*GPE that was charged and discharged at a current density of 0.2 mA cm^{-2} between 2.5 and 4.2 V: (a) capacity and CE in different cycles and (b) charge–discharge profiles in different cycles.